Discrete effects on boundary conditions of the lattice Boltzmann method for fluid flows with curved no-slip walls

Liang Wang,[1,2] Shi Tao ⬦,[3] Xuhui Meng,[4] Kai Zhang,[1,2] and Gui Lu[5,*]

[1]*Beijing Key Laboratory of Emission Surveillance and Control for Thermal Power Generation,*
North China Electric Power University, Beijing 102206, China
[2]*School of Energy Power and Mechanical Engineering, North China Electric Power University, Beijing 102206, China*
[3]*Guangdong Provincial Key Laboratory of Distributed Energy Systems, Dongguan University of Technology, Dongguan 523808, China*
[4]*Division of Applied Mathematics, Brown University, Providence, Rhode Island 02912, USA*
[5]*Key Laboratory of Condition Monitoring and Control for Power Plant Equipment of Ministry of Education,*
North China Electric Power University, Beijing 102206, China

The lattice Boltzmann method (LBM) has been formulated as a powerful numerical tool to simulate incompressible fluid flows. However, it is still a critical issue for the LBM to overcome the discrete effects on boundary conditions successfully for curved no-slip walls. In this paper, we focus on the discrete effects of curved boundary conditions within the framework of the multiple-relaxation-time (MRT) model. We analyze in detail a single-node curved boundary condition [Zhao *et al.*, Multiscale Model. Simul. **17**, 854 (2019)] for predicting the Poiseuille flow and derive the numerical slip at the boundary dependent on a free parameter as well as the distance ratio and the relaxation times. An approach by virtue of the free parameter is then proposed to eliminate the slip velocity while with uniform relaxation parameters. The theoretical analysis also indicates that for previous curved boundary schemes only with the distance ratio and the halfway bounce-back (HBB) boundary scheme, the numerical slip cannot be removed with uniform relaxation times virtually. We further carried out some simulations to validate our theoretical derivations, and the numerical results for the case of straight and curved boundaries confirm our theoretical analysis. Finally, for fluid flows with curved boundary geometries, resorting to more degrees of freedom from the boundary scheme may have more potential to eliminate the discrete effect at the boundary with uniform relaxation times.

I. INTRODUCTION

Over the past two decades, the lattice Boltzmann method (LBM) has been formulated as an effective mesoscopic simulation tool for various hydrodynamic problems [1–6]. Unlike the conventional computational fluid dynamics method, the LBM does not solve the macroscopic variables but instead the discrete distribution functions with the so-called "Collision and Streaming" algorithm [7]. The kinetic nature and local dynamics, which bring about the algorithmic simplicity, easy boundary treatment, and natural parallelism, boost the growing popularity of the LBM to compute fluid flows that are governed by the Navier-Stokes equations. Up to now, there have been considerable kinetic boundary schemes as well as the lattice Boltzmann (LB) equation models in the literature [8,9]. The present discussion treats the special case of the no-slip boundary condition at physical walls.

In the context of the LBM, the boundary condition is responsible for determining the unknown distribution function at the lattice nodes nearest to the physical boundary (i.e., boundary nodes). Among these boundary conditions for

realizing no-slip walls, the bounce-back scheme is the most common and simplest implementation. This scheme requires that the outgoing particle distribution at the boundary node reflects back in the opposite direction [7]. However, it has been recognized that the so-called discrete effects from boundary schemes must be minimized to derive correct results for fluid flows. This important topic has been extensively investigated by many researchers. Ginzburg and Adler [10] analyzed the boundary condition of the face-centered-hypercube LB model and found that for the plane Poiseuille flow, the halfway bounce-back (HBB) boundary condition produces a second-order spatial error, which can be eliminated due to a special relationship complied by some eigenvalues of the collision matrix. He *et al.* [11] conducted an analysis of the discrete effects of several boundary conditions with the Bhatnagar-Gross-Krook (BGK) model and mathematically derived the slip velocities generated in the bounce-back boundary condition. For the Poiseuille flow solved by the three-dimensional BGK model, Prasianakis *et al.* [12] found similar results for the discrete effect of the HBB boundary condition as the two-dimensional case [11]. Following the procedure outlined in Ref. [11], Meng *et al.* [13] recently implemented the analysis for the BGK model with two discrete velocity models and investigated the slip velocity produced by the modified

*Corresponding author: luguI02@gmail.com

bounce-back scheme [11]. To eliminate the nonphysical slip velocity, they provided a strategy to supplement the missed distribution function in the bounce-back scheme. Through the developed Taylor expansion method [14,15], Dubois *et al.* [16] also performed an analysis of the HBB boundary condition within the multiple-relaxation-time (MRT) model for the Poiseuille flow. They obtained the combined relations of relaxation times for the HBB boundary scheme exact up to third order. With the MRT model based on the lattice kinetic scheme [17–19], Meng and Guo [20] analyzed the HBB boundary scheme for the Poiseuille flow and determined the choice of the relaxation rate λ_4 (or λ_6) to realize the no-slip boundary condition. However, we note that the aforementioned boundary condition analyses are restricted to flows with straight boundary geometry, which is located just at the lattice node or halfway away from the boundary node. In addition, it can be noticed that for inclined straight boundaries or curved ones, the distance of a boundary node from physical walls is changeable with its position and link lattice direction. Therefore, the above derivation results for aligned flat walls are theoretically invalid to yield enough accurate results when dealing with curved boundaries.

For fluid flows with curved walls, there have been many boundary conditions based on interpolating or extrapolating the distribution function or the fluid velocity at boundary nodes [9,21]. The exact location of the physical boundary is embodied through its intersection distance ratio γ between boundary nodes and solid nodes. Although being more accurate than the bounce-back treatment for curved walls, some discrete effects still exist in these curved boundary schemes [22–24]. When examining the mass leakage of curved boundary conditions [25,26], Bao *et al.* [22] observed a nonzero velocity in a hydrostatic flow system with the no-slip boundary condition. Such slip velocities associated with γ are also revealed by Oulaid and Zhang in their hydrostatic simulations [23]. Unlike the mathematical expressions of He *et al.* [11], they attributed the slip velocity over the boundary walls to the violation of involved assumptions in the boundary scheme. They further proposed a formulation of modifications to restrain the artificial velocity. Through the Chapman-Enskog expansion and the Taylor expansion, Ginzburg and d'Humières [27] theoretically studied the accuracy of some existing boundary conditions and their multireflection boundary scheme for curved no-slip walls. From the analysis for the simple Poiseuille flow, it is definitely indicated that the numerical error from the exact solution is affected by a combined coefficient of two relaxation parameters plus the distance ratio. In developing second-order volumetric boundary schemes for no-slip walls, Rohde *et al.* [24] analyzed the discrete effect of the bounce-back method for planar Poiseuille flow and skew channel flow. They found that the numerical slip is dependent on the combined effects of the relaxation time and the weighting factor (equivalently, the distance ratio γ). For skew channel flows, their mathematical derivations show that the slip velocity is influenced by the distance ratio γ varied with lattice directions.

From the above available works, we can learn that besides the relaxation parameter, the distance ratio at a boundary node and certain associated linking lattice direction also affects the discrete effects of curved boundary conditions.

Therefore, to eliminate the numerical slip from boundary conditions for curved no-slip walls, the relaxation parameter in the LBM should be changeable at different boundary nodes with different distance ratios. However, these nonuniform relaxation parameters make the collision operator anisotropic. One conventional strategy for this issue is to approximate the curved surface with zigzag lines, which is composed by some points located halfway between the boundary and solid nodes [28,29]. In this way the HBB scheme is executed at boundary nodes for the no-slip boundary condition, and the uniform relaxation parameter then can be determined with the fixed $\gamma = 0.5$ [10,11]. However, such a treatment will lose the fidelity of real curved geometry under coarse grid resolutions, and more importantly, it can still lead to a nonzero numerical slip on the solid wall [30]. Therefore, as noted above, it is inspiring us to resolve the critical issue about the discrete effects of curved boundary conditions: the relaxation parameters are kept invariant while the numerical slip at curved no-slip walls can be removed successfully.

The main objective of this work is, therefore, to keep the relaxation parameters unchanged while the discrete effects on boundary conditions are eliminated for fluid flows with curved no-slip walls. Unlike previous curved boundary conditions, the single-node boundary condition recently proposed by Zhao *et al.* [31] contains another free parameter as well as the distance ratio γ, which can bring many boundary schemes, and hence is adopted in our analysis. As usually done in previous studies, the planar Poiseuille flow is employed as the benchmark problem for the mathematical analysis. We will theoretically deduce the numerical slip associated with the curved boundary scheme within the MRT model, and then show how to eliminate the discrete effect with uniform relaxation parameters. The theoretical analysis is scrutinized by simulating fluid flows with aligned and inclined planar walls and curved walls. Additionally, the HBB boundary scheme is compared with the adopted curved boundary condition in terms of the slip velocity on curved no-slip walls. It is unequivocally found that the present derivations produce the most accurate results consistent with the analytical solution.

The paper is organized as follows. Section II briefly describes the MRT LB model for fluid flows. In Sec. III the adopted single-node boundary condition is first analyzed, and we subsequently show how to achieve uniform relaxation parameters to remove the numerical slip. Some numerical tests and comparisons are performed in Sec. IV, and finally a summary is given in Sec. V.

II. MULTIPLE-RELAXATION-TIME LATTICE BOLTZMANN MODEL FOR FLUID FLOWS

The working principle of the LBM is to track the discrete distribution functions in time and space. The evolution of these distribution functions conforms to the lattice Boltzmann equation (LBE),

$$f_i(\boldsymbol{x} + \boldsymbol{c}_i\delta_t, t + \delta_t) - f_i(\boldsymbol{x}, t) = \Omega_i(f)(\boldsymbol{x}, t) + \delta_t F_i(\boldsymbol{x}, t),$$
$$i = 0, 1, \ldots, b - 1, \qquad (1)$$

where $f_i(\boldsymbol{x}, t)$ is the distribution function at position $\boldsymbol{x}$ and time t moving with the discrete velocity $\boldsymbol{c}_i$, $\Omega_i(f)$ is the

discrete collision operator, F_i is the forcing term, δ_t is the time step, and b is the number of discrete velocities.

Our starting point is the LB model with the MRT collision operator. This is due to the fact that the generalized MRT model possesses more free relaxation parameters and can remedy some numerical artifacts in the BGK model [10,11,27,32]. The MRT collision operator has the following form:

$$\Omega_i(f) = -\sum_j (\boldsymbol{M}^{-1}\boldsymbol{S}\boldsymbol{M})_{ij}\big[f_j - f_j^{(\text{eq})}\big], \qquad (2)$$

where $\boldsymbol{M}$ is a $b \times b$ transformation matrix, and $\boldsymbol{S} = \text{diag}(\tau_0, \tau_1, \ldots, \tau_{b-1})^{-1}$ is a diagonal relaxation matrix with non-negative elements. $f_j^{(\text{eq})}$ appearing in Eq. (2) is the equilibrium distribution function given by

$$f_j^{(\text{eq})} = \omega_j \rho \left[1 + \frac{\boldsymbol{c}_j \cdot \boldsymbol{u}}{c_s^2} + \frac{(\boldsymbol{c}_j \cdot \boldsymbol{u})^2}{2c_s^4} - \frac{\boldsymbol{u}^2}{2c_s^2}\right],$$
$$j = 0, 1, \ldots, b-1, \qquad (3)$$

where ω_j is the weight coefficient, c_s is the lattice sound speed, and ρ and $\boldsymbol{u}$ are, respectively, the density and fluid velocity. To be accurately consistent with the macroscopic equations, the discrete forcing term F_i in Eq. (1) should be taken as [8]

$$\boldsymbol{F} = \boldsymbol{M}^{-1}\left(\boldsymbol{I} - \frac{\boldsymbol{S}}{2}\right)\boldsymbol{M}\overline{\boldsymbol{F}}, \qquad (4)$$

where $\boldsymbol{I}$ is the identity matrix, $\boldsymbol{F} = (F_0, F_1, \ldots, F_{b-1})^{\text{T}}$ is a b-dimensional vector, and $\overline{\boldsymbol{F}} = (\overline{F}_0, \overline{F}_1, \ldots, \overline{F}_{b-1})^{\text{T}}$ is given from the external force $\boldsymbol{G} = \rho\boldsymbol{a}$:

$$\overline{F}_i = \omega_i \rho \left[\frac{\boldsymbol{c}_j \cdot \boldsymbol{a}}{c_s^2} + \frac{\boldsymbol{u}\boldsymbol{a} : (\boldsymbol{c}_i\boldsymbol{c}_i - c_s^2\boldsymbol{I})}{c_s^4}\right]. \qquad (5)$$

In this work, our analyses are carried out in the two-dimensional case. Thus, we consider the D2Q9 (two-dimensional nine-velocity) lattice model where the discrete velocities are given by

$$\boldsymbol{c}_i := c\boldsymbol{e}_i = \begin{cases} c(0,0), & i = 0, \\ c(\cos[(i-1)\pi/2], \sin[(i-1)\pi/2]), & i = 1, 2, 3, 4, \\ \sqrt{2}c(\cos[(i-1)\pi/2 + \pi/4], \sin[(i-1)\pi/2 + \pi/4]), & i = 5, 6, 7, 8, \end{cases} \qquad (6)$$

where $c = \delta_x/\delta_t$ with δ_x denoting the lattice spacing. Correspondingly, the sound speed $c_s = c/\sqrt{3}$, and the weight coefficients are taken as $\omega_0 = 4/9$, $\omega_{1-4} = 1/9$, and $\omega_{5-8} = 1/36$.

In the framework of the MRT model, the transformation matrix $\boldsymbol{M}$ maps the discrete distribution functions f_i onto the moment space $\boldsymbol{m} := \boldsymbol{M}\boldsymbol{f}$ where $\boldsymbol{f} = (f_0, f_1, \ldots, f_8)^{\text{T}}$. It can be constructed from the discrete velocities via the Gram-Schmidt orthogonalization procedure. For the D2Q9 model, one form of the matrix $\boldsymbol{M}$ with $c = 1$ is given by [33]

$$\boldsymbol{M} = \begin{pmatrix} 1 & 1 & 1 & 1 & 1 & 1 & 1 & 1 & 1 \\ -4 & -1 & -1 & -1 & -1 & 2 & 2 & 2 & 2 \\ 4 & -2 & -2 & -2 & -2 & 1 & 1 & 1 & 1 \\ 0 & 1 & 0 & -1 & 0 & 1 & -1 & -1 & 1 \\ 0 & -2 & 0 & 2 & 0 & 1 & -1 & -1 & 1 \\ 0 & 0 & 1 & 0 & -1 & 1 & 1 & -1 & -1 \\ 0 & 0 & -2 & 0 & 2 & 1 & 1 & -1 & -1 \\ 0 & 1 & -1 & 1 & -1 & 0 & 0 & 0 & 0 \\ 0 & 0 & 0 & 0 & 0 & 1 & -1 & 1 & -1 \end{pmatrix}. \qquad (7)$$

As a result, the discrete velocity moments of distribution functions are expressed in the following order:

$$\boldsymbol{m} = \boldsymbol{M}\boldsymbol{f} = (\rho, e, \varepsilon, j_x, q_x, j_y, q_y, p_{xx}, p_{xy})^{\text{T}}. \qquad (8)$$

As noted in Ref. [33], each moment has clear physical significance: ρ is the density stemming from the zero-order moment; e is related to the total energy stemming from the second-order moment; ε is related to the energy square stemming from the fourth-order moment; j_x and j_y are, respectively, the x and y components of momentum stemming from the first-order moments; q_x and q_y are, respectively, the x and y components of energy flux stemming from the third-order moments; p_{xx} and p_{xy} are, respectively, the diagonal and off-diagonal com-

ponents of the stress tensor stemming from the second-order moments. The corresponding relaxation diagonal matrix $\boldsymbol{S}$ has the following relaxation elements:

$$\boldsymbol{S} = \text{diag}(\tau_\rho, \tau_e, \tau_\varepsilon, \tau_j, \tau_q, \tau_j, \tau_q, \tau_s, \tau_s)^{-1}. \qquad (9)$$

The fluid density ρ and velocity $\boldsymbol{u} = (u, v)$ are computed by the distribution function

$$\rho = \sum_i f_i, \quad \rho\boldsymbol{u} = \sum_i \boldsymbol{c}_i f_i + \frac{\delta_t}{2}\rho\boldsymbol{a}. \qquad (10)$$

Through the multiscale analysis as demonstrated in much of the literature, the MRT model with the above equilibria (3) and the forcing term (5) can derive the Navier-Stokes equations:

$$\partial_t \rho + \nabla \cdot (\rho\boldsymbol{u}) = 0, \qquad (11\text{a})$$

$$\partial_t(\rho\boldsymbol{u}) + \nabla \cdot (\rho\boldsymbol{u}\boldsymbol{u}) = -\nabla p + \nabla \cdot [2\rho\nu\boldsymbol{S}$$
$$+ \rho\zeta(\nabla \cdot \boldsymbol{u})\boldsymbol{I}] + \rho\boldsymbol{a}, \qquad (11\text{b})$$

where $p = c_s^2\rho$ is the fluid pressure, $\boldsymbol{S} = [\nabla\boldsymbol{u} + (\nabla\boldsymbol{u})^{\text{T}}]/2$ is the strain rate, and the shear and bulk viscosities are, respectively, determined by

$$\nu = c_s^2\big(\tau_s - \tfrac{1}{2}\big)\delta_t, \quad \zeta = c_s^2\big(\tau_e - \tfrac{1}{2}\big)\delta_t. \qquad (12)$$

The implementation of Eq. (1) can be decomposed into two substeps:

Collision:
$$f_i'(\boldsymbol{x}, t) = f_i(\boldsymbol{x}, t)$$
$$- \sum_j (\boldsymbol{M}^{-1}\boldsymbol{S}\boldsymbol{M})_{ij}\big[f_j(\boldsymbol{x}, t) - f_j^{(\text{eq})}(\boldsymbol{x}, t)\big]$$
$$+ \delta_t F_i(\boldsymbol{x}, t),$$

Streaming:
$$f_i(\boldsymbol{x} + \boldsymbol{c}_i\delta_t, t + \delta_t) = f_i'(\boldsymbol{x}, t), \qquad (13)$$
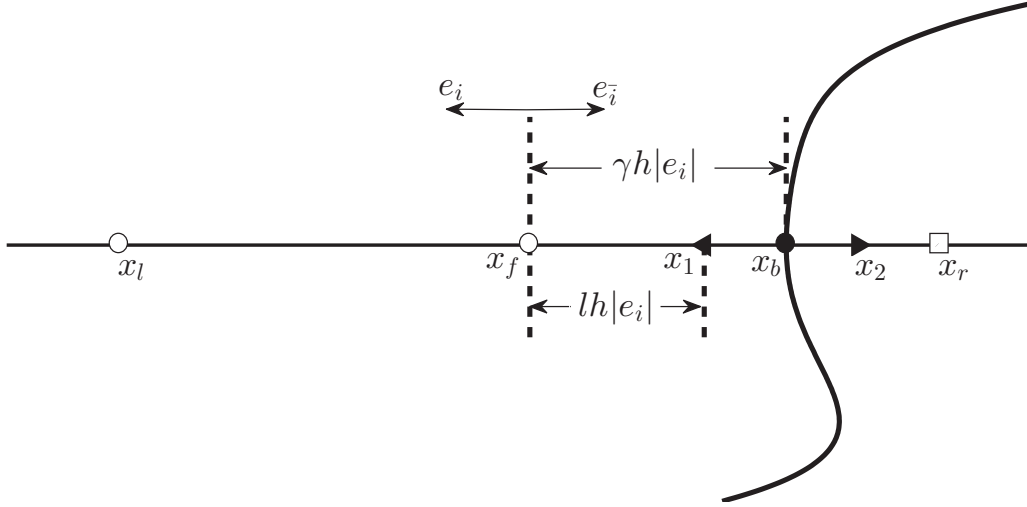
FIG. 1. Schematic of a curved-wall boundary along one single lattice direction. The thin solid line is the grid line, and the thick curved one represents the boundary surface. White circles ($\circ$): the fluid nodes; black circle ($\bullet$): the intersection point of the boundary with the grid line; square box ($\square$): the solid node outside the computational domain.

where $f_i'(\boldsymbol{x}, t)$ is the postcollision distribution function. In the framework of the MRT model, the collision step is usually executed in the moment space first and then mapped to the velocity space:

$$\boldsymbol{m}'(\boldsymbol{x}, t) = \boldsymbol{m}(\boldsymbol{x}, t) - \boldsymbol{S}[\boldsymbol{m}(\boldsymbol{x}, t) - \boldsymbol{m}^{(\text{eq})}(\boldsymbol{x}, t)] + \delta_t \hat{\boldsymbol{F}}(\boldsymbol{x}, t),$$

$$\boldsymbol{f}'(\boldsymbol{x}, t) = \boldsymbol{M}^{-1} \boldsymbol{m}'(\boldsymbol{x}, t),$$

$$(14)$$

where $\boldsymbol{m}' := \boldsymbol{M}\boldsymbol{f}'$ with $\boldsymbol{f}' = (f_0', f_1', \ldots, f_8')^{\text{T}}$ denotes the postcollision moment, and $\boldsymbol{m}^{(\text{eq})} := \boldsymbol{M}\boldsymbol{f}^{(\text{eq})}$ and $\hat{\boldsymbol{F}} := \boldsymbol{M}\boldsymbol{F} = (\boldsymbol{I} - \frac{\boldsymbol{S}}{2})\hat{\bar{\boldsymbol{F}}}$ are the corresponding equilibria and forcing term in the moment space, respectively. Finally, it should be noted that when the relaxation times are equal to the same τ, i.e., $\boldsymbol{S} = \frac{1}{\tau}\boldsymbol{I}$, the MRT model will reduce to the BGK model.

III. SINGLE-NODE BOUNDARY CONDITION FOR CURVED NO-SLIP WALLS

In addition to the LB models for the evolution of distribution functions, boundary conditions play another important role in simulating fluid flows by the LBM. For a more accurate treatment of curved no-slip walls, the tunable distance ratio γ is commonly included in various curved boundary schemes rather than the HBB scheme in the literature [7–9]. However, when the discrete effects are removed from these boundary conditions, the relaxation parameters, as noted previously, cannot be independent of γ at boundary nodes with different lattice directions. To resolve this important problem, we will analyze a single-node curved boundary condition within the framework of the MRT model first, and then provide our strategy to eliminate the discrete effect with uniform relaxation parameters.

A. The single-node boundary condition for a curved no-slip wall

To adapt with the local computation of the LBM, our subsequent analyses are based on single-node boundary schemes,

which involve only the information of the current boundary node without invoking interpolation or extrapolation treatments. Actually, for flows with curved boundaries or porous flows, such local single-node boundary treatments would be especially desired.

Note that the no-slip boundary condition with a curved wall can be treated separately for each lattice direction along a boundary node. For the sake of convenience, we consider a single lattice direction $\boldsymbol{e}_i$ from the intersected point $\boldsymbol{x}_b$ to the boundary node $\boldsymbol{x}_f$, as illustrated in Fig. 1. The curved wall intersected with the link of boundary node $\boldsymbol{x}_f$ and solid node $\boldsymbol{x}_r$ is depicted using the distance ratio γ as $\gamma = |\boldsymbol{x}_b - \boldsymbol{x}_f|/|\boldsymbol{x}_r - \boldsymbol{x}_f|$. For the no-slip boundary condition on the curved wall, the fluid velocity $\boldsymbol{u}(\boldsymbol{x}, t)$ obtained from the Navier-Stokes equations at $\boldsymbol{x}_b$ should equal the wall velocity $\boldsymbol{u}(\boldsymbol{x}_b, t)$. As displayed in Fig. 1, after a time step δ_t, the distribution function $f_i(\boldsymbol{x}_f, t + \delta_t)$ at $\boldsymbol{x}_f$ in lattice direction $\boldsymbol{e}_i$ is unknown and to be determined. To this end, the single-node boundary condition developed by Zhao *et al.* [31] is adopted to give the unknown distribution function $f_i(\boldsymbol{x}_f, t + \delta_t)$:

$$f_i(\boldsymbol{x}_f, t + \delta_t) = \frac{1 + l - 2\gamma}{1 + l} f_i(\boldsymbol{x}_f, t) + \frac{l}{1 + l} f_i'(\boldsymbol{x}_f, t)$$

$$+ \frac{2\gamma - l}{1 + l} f_{\bar{i}}'(\boldsymbol{x}_f, t) + \frac{2}{1 + l} \omega_i \rho_0 \frac{\boldsymbol{c}_i \cdot \boldsymbol{u}(\boldsymbol{x}_b, t)}{c_s^2},$$

$$(15)$$

where $\bar{i}$ results in $\boldsymbol{e}_{\bar{i}} = -\boldsymbol{e}_i$, ρ_0 is the mean density, and l is a free parameter. In Ref. [31], l is introduced such that $\boldsymbol{x}_b = (\boldsymbol{x}_1 + \boldsymbol{x}_2)/2$ for using the HBB scheme. To achieve the convex combination in Eq. (15) for numerical stability, the parameter l should obey the condition of $\max\{0, 2\gamma - 1\} \leqslant l \leqslant 2\gamma$ as given in Ref. [31]. It can be seen that no information from other neighboring nodes of $\boldsymbol{x}_f$ is involved in this boundary scheme. Under the diffusive scaling $\delta_t = \eta h^2$, $h = \delta_x$ (η is an adjustable parameter), the single-node scheme has been justified to be second-order accurate in space [31].
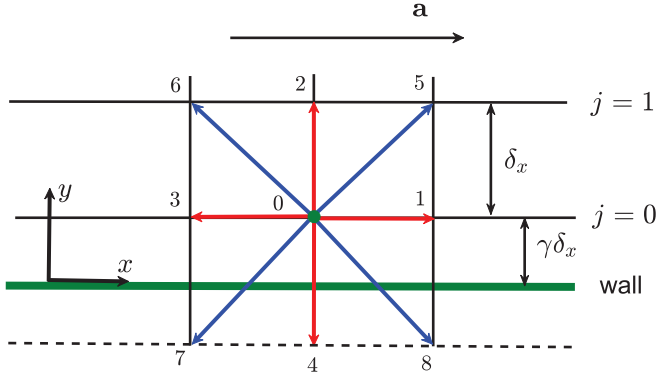
FIG. 2. Schematic of the flow and lattice arrangement with a distance ratio γ. The wall boundary in the HBB boundary condition is placed with $\gamma = 1/2$.

In previous boundary conditions for a curved no-slip wall, most of them contain only the distance ratio γ as a variable parameter. In contrast, the above adopted boundary scheme contains another free parameter l as well as γ. Because of the flexibility of l, numerous curved boundary conditions, including some existing single-node schemes, can be generated. For example, the HBB scheme [28] corresponds to $l = 0$, $\gamma = 0.5$ in Eq. (15). More importantly, as will be shown later, it is the free parameter l that ensures the invariant relaxation parameters when the discrete effect is removed.

B. Discrete effect on the single-node boundary scheme

We now examine the discrete effect of the boundary scheme expressed by Eq. (15). To simplify the analysis, we will consider a unidirectional incompressible flow problem, i.e., the force-driven Poiseuille flow in a channel, which has been commonly adopted in previous studies [10,11,13,16,20,27]. This time-independent problem, as shown in Fig. 2, has the following assumptions:

$$\rho = \text{const}, \quad v = 0, \quad \partial_x \phi = 0, \quad \partial_t \phi = 0, \quad (16)$$

where ϕ is an arbitrary flow variable. Without loss of generality, the planar wall is kept stationary, i.e., $\boldsymbol{u}(\boldsymbol{x}_b) = \boldsymbol{0}$. The driven force is assigned with a constant acceleration $\boldsymbol{a} = (a, 0)$ along the x direction. The wall boundary locates with a distance ratio of γ away from its nearest inner lattice node at $j = 0$. Here j is the index of the grid line at $y_j = (j + \gamma)\delta_x$. After the streaming step, the distribution functions $f_0, f_1, f_3, f_4, f_7,$ and f_8 at the layer $j = 0$ are known, while the remaining inward ones, $f_2, f_5,$ and f_6, are unknown and determined from Eq. (15):

$$f_2^0 = \frac{1 + l - 2\gamma}{1 + l} f_4^0 + \frac{l}{1 + l} f_2'^0 + \frac{2\gamma - l}{1 + l} f_4'^0, \quad (17a)$$

$$f_5^0 = \frac{1 + l - 2\gamma}{1 + l} f_7^0 + \frac{l}{1 + l} f_5'^0 + \frac{2\gamma - l}{1 + l} f_7'^0, \quad (17b)$$

$$f_6^0 = \frac{1 + l - 2\gamma}{1 + l} f_8^0 + \frac{l}{1 + l} f_6'^0 + \frac{2\gamma - l}{1 + l} f_8'^0, \quad (17c)$$

where $f_i^0 = f_i(y_0)$ and $f_i'^0 = f_i'(y_0)$ with $y_0 = \gamma \delta_x$.

Before proceeding to derive the numerical slip from Eq. (17), we can obtain the following formulas based on the relationship between $\boldsymbol{f}$ and $\boldsymbol{m}$:

$$f_1 - f_3 = \frac{1}{3} j_x - \frac{1}{3} q_x, \quad (18a)$$

$$f_5 - f_6 = \frac{1}{3} j_x + \frac{1}{6} q_x + \frac{1}{2} p_{xy}, \quad (18b)$$

$$f_8 - f_7 = \frac{1}{3} j_x + \frac{1}{6} q_x - \frac{1}{2} p_{xy}, \quad (18c)$$

from which together with Eq. (10) we can have

$$j_x = \rho u - \frac{1}{2} \delta_t \rho a. \quad (19)$$

In a similar way, the postcollision distribution functions can be expressed as follows:

$$f_1' - f_3' = \frac{1}{3} j_x' - \frac{1}{3} q_x', \quad (20a)$$

$$f_5' - f_6' = \frac{1}{3} j_x' + \frac{1}{6} q_x' + \frac{1}{2} p_{xy}', \quad (20b)$$

$$f_8' - f_7' = \frac{1}{3} j_x' + \frac{1}{6} q_x' - \frac{1}{2} p_{xy}', \quad (20c)$$

where j_x', q_x', and p_{xy}' stand for the postcollision moments. Accompanied by the conditions in Eq. (16), we can obtain that

$$j_x^{(eq)} = \rho u, \quad q_x^{(eq)} = -\rho u, \quad p_{xy}^{(eq)} = 0, \quad (21a)$$

$$\hat{\bar{F}}_3 = \rho a, \quad \hat{\bar{F}}_4 = -\rho a, \quad \hat{\bar{F}}_8 = 0. \quad (21b)$$

Then, on the basis of Eq. (14), the postcollision moments j_x', q_x', and p_{xy}' can be expressed as follows:

$$j_x' = \left(1 - \frac{1}{\tau_j}\right) j_x + \frac{1}{\tau_j} \rho u + \left(1 - \frac{1}{2\tau_j}\right) \rho a \delta_t, \quad (22a)$$

$$q_x' = \left(1 - \frac{1}{\tau_q}\right) q_x - \frac{1}{\tau_q} \rho u - \left(1 - \frac{1}{2\tau_q}\right) \rho a \delta_t, \quad (22b)$$

$$p_{xy}' = \left(1 - \frac{1}{\tau_s}\right) p_{xy}. \quad (22c)$$

Applying the unidirectional property of the flow, it suggests that

$$f_1 - f_3 = f_1' - f_3'. \quad (23)$$

Further based on Eqs. (18a), (19), (20a), and (22), we can obtain

$$q_x = -\rho u_x - \left(2\tau_q - \frac{1}{2}\right) \rho a \delta_t, \quad (24)$$

from which combined with Eq. (19) we can derive that

$$j_x' = \rho u + \frac{1}{2} \rho a \delta_t, \quad (25a)$$

$$q_x' = -\rho u - \left(2\tau_q - \frac{3}{2}\right) \rho a \delta_t. \quad (25b)$$

In order to obtain the numerical slip due to discrete effects, we now turn to the single-node boundary scheme given by

Eq. (17). First, based on the relationship between the distribution functions at $j = 0$ and $j = 1$ (see Fig. 2), we have

$$f_5^1 - f_6^1 = f_5^{\prime 0} - f_6^{\prime 0}, \quad f_8^0 - f_7^0 = f_5^{\prime 1} - f_6^{\prime 1}, \quad (26)$$

where $f_i^j = f_i(y_j)$ and $f_i^{\prime j} = f_i^\prime(y_j)$. With the above results at hand, we can deduce p_{xy}^0 from Eq. (26) that

$$p_{xy}^0 = \frac{\tau_s[(2\tau_s - 1)(\rho u_0 - \rho u_1) - 3\rho a \delta_t]}{3(2\tau_s - 1)}, \quad (27)$$

where $u_j = u(y_j)$. Furthermore, we can obtain the following relationship as Eq. (17) is employed:

$$\frac{1 + l - 2\gamma}{1 + l}\left(f_8^0 - f_7^0\right) + \frac{2\gamma - l}{1 + l}\left(f_8^{\prime 0} - f_7^{\prime 0}\right)$$
$$= \frac{l}{1 + l}\left(f_5^{\prime 0} - f_6^{\prime 0}\right) - \left(f_5^0 - f_6^0\right). \quad (28)$$

After some tedious manipulations, one can derive another expression of p_{xy}^0 as

$$p_{xy}^0 = -\frac{\tau_s}{3\gamma}\rho u_0 + \frac{\tau_s(1 + 4\tau_q + 6l - 6\gamma)}{6\gamma}\rho a \delta_t. \quad (29)$$

Equating Eq. (27) and Eq. (29), one can reach the relationship between u_0 and u_1,

$$u_1 = A u_0 + B a \delta_t, \quad (30)$$

where

$$A = \frac{1 + \gamma}{\gamma},$$
$$B = \frac{-6l(2\tau_s - 1) + 12\gamma(\tau_s - 1) - (1 + 4\tau_q)(2\tau_s - 1)}{2\gamma(2\tau_s - 1)}. \quad (31)$$

As for the considered Poiseuille flow, due to discrete effects of boundary conditions, the LB results will deviate from the analytical solution with a numerical slip. Thus, the fluid velocity predicted between two flat plates, which are located at $y = 0$ and $y = H$, can be written as

$$u_j = 4 u_c \frac{y_j}{H}\left(1 - \frac{y_j}{H}\right) + u_s, \quad (32)$$

where $u_c = a H^2 / 8\nu$ is the maximum sreamwise velocity, and u_s is the slip velocity at the solid wall. By substituting Eq. (32) at $j = 0$ and $j = 1$ into Eq. (30), we can obtain the dimensionless slip velocity:

$$U_s := \frac{u_s}{u_c} = \frac{2}{3}\frac{\delta_x^2}{H^2}[-6\gamma^2 + 6\gamma(1 - 2\tau_s) + 6l(2\tau_s - 1)$$
$$+ (1 + 4\tau_q)(2\tau_s - 1)]. \quad (33)$$

Here we comment on the results derived above. First, when the wall moves with a velocity $\boldsymbol{u}(\boldsymbol{x}_b)$, by following the above analysis procedure, the expression of the slip velocity can be still derived as Eq. (33). Second, the slip velocity U_s generated in the boundary scheme (17) has a quadratic dependence on δ_x / H. This clearly confirms the second-order accuracy of the single-node scheme (15) as justified by Zhao *et al.* [31]. Third, when the parameter l is dependent only on γ, the slip velocity U_s degenerates to be related to the relaxation times and the distance ratio γ, which is the current practice

in previous curved boundary conditions. From this viewpoint, we now could have more degree of freedom to eliminate U_s than previous studies. The last and final point is that, as noted in Ref. [31], the parameter l in Eq. (17) is such that $\boldsymbol{x}_b = (\boldsymbol{x}_1 + \boldsymbol{x}_2)/2$ in the link along direction $\boldsymbol{e}_i$ (see Fig. 1). Thus, the free parameter l should be considered as a function of γ.

C. Elimination of the slip velocity

Now we focus on how to eliminate the slip velocity to realize the no-slip boundary condition on curved walls. To this end, we let $U_s = 0$ in Eq. (33) and obtain that

$$U_s = 0 \Rightarrow \tau_q = \frac{1 + 6l - 6\gamma + 6\gamma^2 - 2\tau_s - 12l\tau_s + 12\gamma\tau_s}{4(2\tau_s - 1)}, \quad (34a)$$

$$l = 0, \quad U_s = 0 \Rightarrow \tau_q = \frac{1 - 6\gamma + 6\gamma^2 - 2\tau_s + 12\gamma\tau_s}{4(2\tau_s - 1)}. \quad (34b)$$

For convenience of description, the slip velocity under $l = 0$ is presented temporarily to correspond to previous study results. In the LBM algorithm, it is known that the relaxation times should be invariant at all the computational nodes. Because the distance ratio γ is fixed in a flat wall boundary, this requirement can be fulfilled for the relaxation time τ_q determined from Eq. (34). However, for a curved wall, it is noted that the distance ratio γ will change its value at different boundary nodes along different lattice directions. Consequently, if the discrete effects are removed from curved boundary conditions, the relaxation time τ_q as determined by Eq. (34b) should be inevitably changeable without the parameter l in previous studies. In contrast, as revealed from Eq. (34a), the relaxation time τ_q in the present analysis is jointly determined by γ and l. The degree of freedom from l would provide us with an opportunity to obtain uniform τ_q. In the following, we will provide our detailed approach to realize this point.

As noted above, the parameter l is a function of γ. For a concrete flow problem, the relaxation time τ_s corresponds to the fluid viscosity [Eq. (12)] and thus should be a constant. Then the numerator of Eq. (34a) is denoted as $P(\gamma) = 6l(1 - 2\tau_s) + 6\gamma^2 + 6\gamma(2\tau_s - 1) + 1 - 2\tau_s$. If the relaxation time τ_q is uniform and independent of γ, $P(\gamma)$ is forced to satisfy $\frac{dP(\gamma)}{d\gamma} = 0$, and thus we have

$$\frac{dP(\gamma)}{d\gamma} = 0 \Rightarrow (1 - 2\tau_s)\frac{dl}{d\gamma} + 2\gamma + (2\tau_s - 1) = 0. \quad (35)$$

The solution to the above ordinary differential equation is

$$l = \frac{\gamma^2 + \gamma(2\tau_s - 1)}{2\tau_s - 1} + C, \quad (36)$$

where C is a constant irrelevant to γ. By substituting the solved l into Eq. (34a), it is interesting but unsurprising that we obtain the uniform relaxation time τ_q:

$$\tau_q = -\frac{1 + 6C}{4}. \quad (37)$$

In summary, as the parameter l is given by Eq. (36), the relaxation time τ_q can take uniform values as expressed by Eq. (37),

and meanwhile the discrete effect of the boundary conditions can be successfully eliminated, i.e., $U_s = 0$. We would like to note that the present treatment cannot be accomplished in previous studies noted before for curved no-slip walls.

Within the BGK model framework, the slip velocity U_s with $l = 0$ is then expressed from Eq. (33) by taking $\tau_s = \tau_q = \tau$:

$$U_s = \frac{2}{3}\frac{\delta_x^2}{H^2}[8\tau^2 - 2\tau - 12\gamma\tau - 1 + 6\gamma - 6\gamma^2], \quad (38)$$

which is similar to those derived in Ref. [24]. Correspondingly, the relaxation time τ to eliminate the discrete effect can be solved from $U_s = 0$:

$$\tau = \frac{1 - 6\gamma + \sqrt{84\gamma^2 - 36\gamma + 9}}{8}. \quad (39)$$

From Eq. (39) we clearly see that to ensure $U_s = 0$ without the free parameter l, the relaxation time in Ref. [24] must be changeable with the distance ratio γ.

As for the above results, we have the following remarks.

Remark 1. Equation (34) at $\gamma = \frac{1}{2}$ determines the relaxation time τ_q to remove the slip velocity of the halfway boundary scheme. Especially, when $\gamma = \frac{1}{2}$ in Eq. (34b), the relaxation time τ_q corresponding to the HBB scheme takes the uniform value as

$$\tau_q = \frac{4\tau_s - \frac{1}{2}}{4(2\tau_s - 1)}, \quad (40)$$

which is consistent with those given in Refs. [10,32].

Remark 2. From Eqs. (34b) and (39), one can find that for a curved boundary scheme without the parameter of l, a uniform relaxation time to ensure $U_s = 0$ cannot be achieved even by extending from the BGK model to the MRT model.

Remark 3. According to the stability condition required in the MRT model [33], τ_q in Eq. (37) should be $\tau_q > \frac{1}{2}$, and thus the constant C should satisfy $C < -\frac{1}{2}$. In addition, to ensure the stability of the boundary scheme (15) as given in Ref. [31], the constant C should be further constrained such that the parameter l in Eq. (36) locates in the region of $\max\{0, 2\gamma - 1\} \leqslant l \leqslant 2\gamma$.

It can be speculated from Eq. (34a) that as γ is near zero, the relaxation time τ_q approximates to $\tau_q = -\frac{1+6l}{4}$ and hence requires that $l < -0.5$. On the other hand, when $\gamma \to 0$, the parameter l approaches zero to match the stability condition as mentioned above for the scheme (15). In this case, it seems hard for the boundary scheme (15) to possess both the numerical stability and the accurate implementation of the boundary condition. For the particular case when $l = 0$, because of the stability requirements that $\tau_s > 0.5$, $\tau_q > 0.5$, one cannot eliminate the slip velocity U_s [Eq. (33)] rigorously as γ is very small. In this paper, to maintain the balance between the twofold points, we compulsively set the parameter $l = 0$ once if $l < -0.4$ obtained from Eq. (36) at very small γ. It is noted that such choice of l is empirically obtained in simulations of the aligned Poiseuille flow, as will be shown later. As will be shown in the following numerical tests, good predictions with the analytical solution can be unambiguously achieved from this compromised treatment. However, as l at small values of γ is not so smaller than zero, the above-mentioned case will not occur.

Finally, it is necessary to give some comments about the elimination of discrete effects from curved boundary conditions. First, although the relaxation time τ_q can be uniform in the HBB boundary condition ($\gamma = \frac{1}{2}$), the midway approximation of boundary nodes essentially degrades the accuracy for general curved geometry. Under coarse grid resolutions, the HBB scheme with Eq. (40) may bring undesired errors, as shown elsewhere [30,32,34]. Second, owing to the local γ at each boundary node, curved boundary schemes can overcome the lost fidelity of real geometry in the HBB scheme. However, if one seeks $U_s = 0$ without the help of l, as clearly shown above, the relaxation time τ_q must be changeable with the distance ratio γ. From a precise point of view, the slip velocity on the curved no-slip wall cannot be removed in the HBB scheme and previous curved boundary schemes only including γ. Third, the proposed treatment is theoretically derived for the Poiseuille flow in an aligned channel. However, it may be applicable to a general flow with curved walls if a second-order polynomial can be assumed to capture the velocity profile locally in the near-wall region. This assumption is reasonable, and the resulting satisfactory results have been demonstrated in some previous studies [24,27,32]. Finally, only by resorting to more degrees of freedom from the relaxation parameter in the LBE (e.g., from the BGK model to the MRT model), it is impractical to accomplish the uniform relaxation time when eliminating the slip velocity on curved no-slip walls. To resolve such a significant problem, one available approach based on our analysis is by introducing additional parameters into the curved boundary scheme.

IV. NUMERICAL RESULTS AND DISCUSSIONS

In this section, we will carry out some numerical tests to validate the above theoretical analysis. All the considered problems have analytical solutions, including the aligned and inclined plane Poiseuille flow and the cylindrical Couette flow. In the simulations, the single-node boundary scheme (15) is employed for the no-slip boundary condition on solid walls. To make comparisons with previous studies, some choices of l besides the present derivation are investigated for the discrete effects on boundary conditions. The slip velocity resulting from HBB boundary scheme is also estimated for curved walls.

For the D2Q9 lattice model considered, τ_ρ and τ_j correspond to the conserved moments and are set as $\tau_\rho = \tau_j = 1.0$,
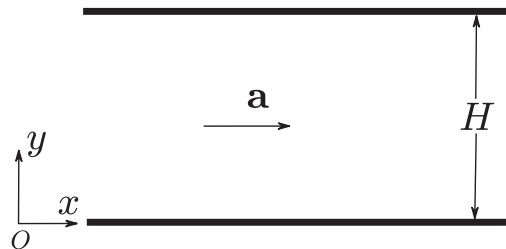

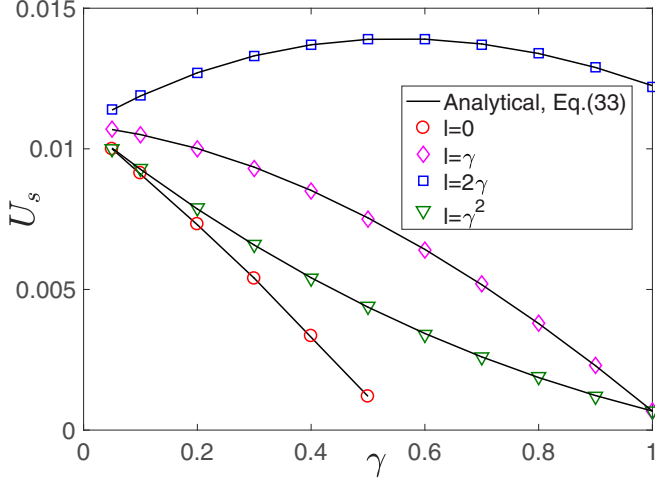FIG. 3. Schematic of the Poiseuille flow between two aligned straight walls.

FIG. 4. Slip velocity as a function of γ under different l at $M = 20$ and Re $= 10$. Solid lines denote the slip velocity derived theoretically [Eq. (33)], and symbols denote the predicted slip velocity from numerical simulations.

τ_s is related to the viscosity and given by Eq. (12), and τ_e and τ_ε are specified as $\tau_e = 1.1$ and $\tau_\varepsilon = 1.0$. As noted elsewhere [10,32], the relaxation time τ_q affects the accurate implementation of the boundary condition. It is determined by Eq. (34), and concretely Eqs. (36) and (37) in our derivations, to ensure $U_s = 0$. Note that the slip velocity expressed by Eq. (33) has a second-order dependence with δ_x. To clearly expose the effect of the numerical slip, numerical simulations are performed under relatively coarse grid resolutions in all the considered problems.

Since the boundary scheme (15) is derived incorporating the diffusive scaling [31], the lattice spacing δ_x and time step δ_t have the relationship $\delta_t = \eta \delta_x^2$ in the simulations, which are

given by

$$\delta_t = \eta \delta_x^2, \quad \eta = \frac{\left(\tau_s - \frac{1}{2}\right)}{3\nu}. \tag{41}$$

A. Force-driven Poiseuille flow

The Poiseuille flow driven by an external force between two straight plates is simulated in this subsection. This benchmark problem has been extensively studied by many researchers using the LBM. Two cases of boundary configurations, i.e., aligned and inclined with the computational grid, are successively considered in the simulations.

1. Aligned channel

The schematic of the flow is shown in Fig. 3, where the driven force is along the x direction with a constant acceleration $\boldsymbol{a} = (a, 0)$. The channel has the width of H, and its inner flow is periodic in the horizontal direction. For this classical problem, the analytical solution is expressed as

$$u = u(y) = 4u_c \frac{y}{H}\left(1 - \frac{y}{H}\right), \quad v = 0, \tag{42}$$

where $y \in [0, H]$, and $u_c = aH^2/8\nu$ is the maximum streamwise velocity. The dimensionless Reynolds number Re is defined as Re $= u_c H/\nu$.

In the simulations, the lower and upper plates are away from boundary nodes with distance $\gamma \delta_x$, as illustrated in Fig. 2. Further, with the grid number M spanning in the vertical direction, the lattice spacing is determined as $\delta_x = H/(M + 2\gamma)$. The simulated slip velocities as a function of γ under different values of l are shown in Fig. 4 where $M = 20$ and Re $= 10$. Here the relaxation time is $\tau_s = 1.2$, $\nu = 0.01$, $H = 1.0$, and $u_c = 0.1$. It is clearly seen that the numerical predictions agree well with the theoretical results given by Eq. (33). In addition, as exhibited in the figure, computations of the boundary scheme (15) with $l = 0$ will collapse as
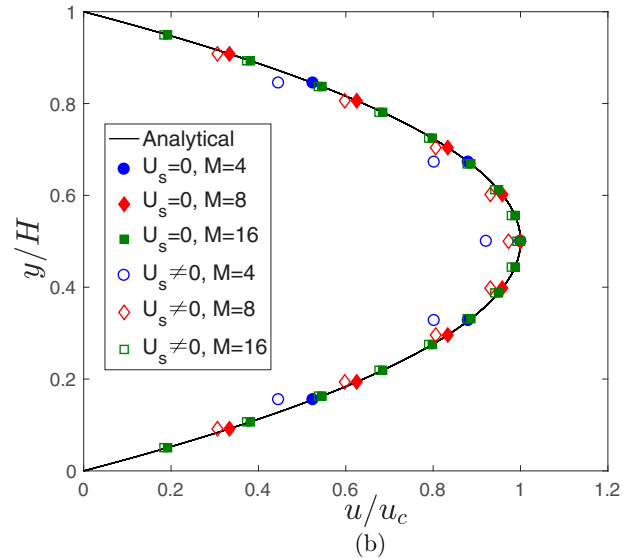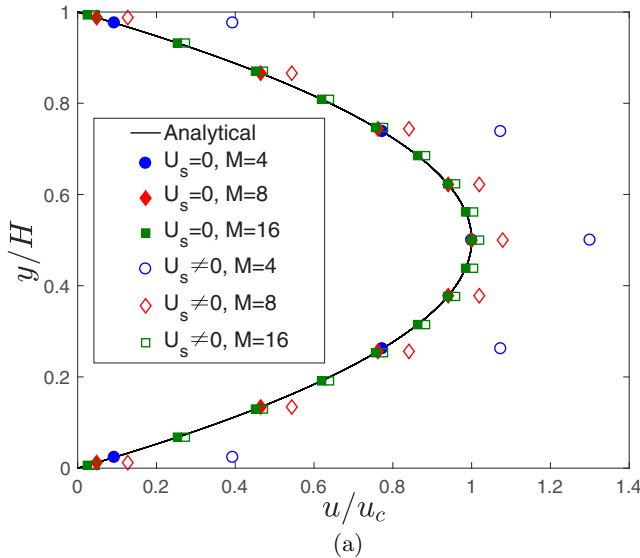

FIG. 5. Velocity profiles predicted from the present analysis with different lattice sizes and (a) $\gamma = 0.1$, (b) $\gamma = 0.9$. Filled shapes denote the results obtained under $U_s = 0$, i.e., Eqs. (36) and (37) with $C = -0.55$. Empty shapes denote the results obtained under $U_s \neq 0$ with $C = -0.55$. Concretely, Eq. (36) and $\tau_q = 100$ are employed for the case of (a) while $l = 0.6$ and Eq. (37) for the case of (b).

TABLE I. Relative errors of velocity $\boldsymbol{u}$ against different values of γ for Re = 1, 10, and 20. Two cases of l ($l = \gamma$, γ^2) are adopted for simulations with the boundary scheme (15).

γ	$\times 10^{-3}$ E_r ($l = \gamma$)			$\times 10^{-3}$ E_r ($l = \gamma^2$)		
	Re = 1	Re = 10	Re = 20	Re = 1	Re = 10	Re = 20
0.05	60.49436	60.52825	60.63210	56.76711	56.79822	56.89366
0.2	54.28215	54.31003	54.39570	42.61098	42.63035	42.69035
0.4	43.69338	43.71264	43.77235	27.76724	27.77637	27.80561
0.6	31.22895	31.24099	31.27916	16.69213	16.69647	16.71184
0.8	17.50761	17.51428	17.53708	8.631314	8.634100	8.646526
1.0	2.979669	2.983320	3.006780	2.979669	2.983320	3.006780

$\gamma > 0.5$. The reason for this instability is ascribed to the nonconvex combination of the distributions in the scheme at $l = 0$ [31,35]. Noteworthily, for some other different Re and M, similar agreement results with the analytical derivation as shown in Fig. 4 are also obtained.

The discrete effects in the boundary condition are also investigated. As has been derived and noted previously, due to the uniform γ equipped in the aligned channel flow, the slip velocity can be overcome for the HBB and curved boundary scheme while with uniform relaxation time. Next, we concentrate on the simulation results from the present analysis, as depicted in Fig. 5. As seen from the figure, it is clear that if the parameter l is given by Eq. (36) together with τ_q by Eq. (37), the results of the boundary scheme (15) can agree excellently with the analytical solution even with a very small grid number (e.g., $M = 4$). In contrast, if l and τ_q are not simultaneously determined from Eqs. (36) and (37) to ensure $U_s = 0$, some grid-dependent results will deviate apparently from the exact velocity profiles. It should be noted that similar results about the discrete effects also occur for the HBB scheme and the curved boundary scheme with the only contained γ.

Based on Re and Eq. (41), the Mach number Ma, which factors in compressibility behavior of fluids, can be expressed as

$$\text{Ma} = \frac{u_c}{c_s} = \frac{\text{Re}\left(\tau_s - \frac{1}{2}\right)}{\sqrt{3}(M + 2\gamma)}. \tag{43}$$

To investigate the effect of Ma on the simulation results, the following relative L^2 error of fluid velocity is used,

$$E_r = \frac{\sqrt{\sum_x |\boldsymbol{u}_a(\boldsymbol{x}) - \boldsymbol{u}_n(\boldsymbol{x})|^2}}{\sqrt{\sum_x |\boldsymbol{u}_a(\boldsymbol{x})|^2}}, \tag{44}$$

where $\boldsymbol{u}_a$ and $\boldsymbol{u}_n$ denote the analytical and numerical results, and the summation is over the entire gird points. Different values of Ma at one γ is obtained via Eq. (43) by varying Re in the simulations, where τ_s is set to 1.2 and $M = 10$. Table I presents the relative errors E_r computed with three different values of Re (Re = 1, 10, 20) under two cases of l ($l = \gamma$, γ^2). As exposed in the table, the relative errors of velocity $\boldsymbol{u}$ increase with the increase of Re (and Ma). This is because that as Ma increases, the compressible effect becomes more prominent, and thus the errors in the simulations will increase. For the same reason, it is seen that the relative errors become larger as γ decreases to increase the Mach number. However, as the simulations conform to the assumption of

low Ma number, good agreement results with the analytical solution still can be obtained.

The stability of the adopted boundary scheme is also investigated as the free parameter l is given by Eq. (36). Figure 6 shows the dependence of l_0 on γ and τ_s, where l_0 is denoted as $l_0 = \frac{\gamma^2 + \gamma(2\tau_s - 1)}{2\tau_s - 1}$ and then $l = l_0 + C$. It is seen that as γ approaches zero, l_0 will be near zero and then l approximates C. At this point, the requirement $\tau_q > 0.5$ in Eq. (37) leads to $C < -0.5$ and further $l < -0.5$. On the other hand, the stability of the boundary scheme (15) limits l in the range of max$\{0, 2\gamma - 1\} \leqslant l \leqslant 2\gamma$ [31], which implies $l \to 0$ as $\gamma \to 0$. Therefore, an artificial choice of l, as noted before, should be used to compromise these twofold points at very small γ. Furthermore, it is deduced that the value of C cannot be far smaller than -0.5 to preserve numerical stability at small γ. It is also observed that l_0 will decrease as τ_s increases, and with $C < -0.5$, l may thus become negative enough to induce numerical unstability at a small γ. In addition, as τ_s approaches 0.5 and γ is close to 1.0, l_0 will be very large such that l would be considerably beyond 2γ, which means the possible instability. To see this analysis more clearly, we check the work status of code computations with the proposed Eq. (36) for l under different γ and τ_s. In the tests, the values of γ range from 0.1 to 1.0, and six values of τ_s ($\tau_s = 0.505, 0.51, 0.52, 0.55, 0.6, 0.65$) are used. The measured results at Re = 10 and $M = 20$ are shown in Fig. 7, where
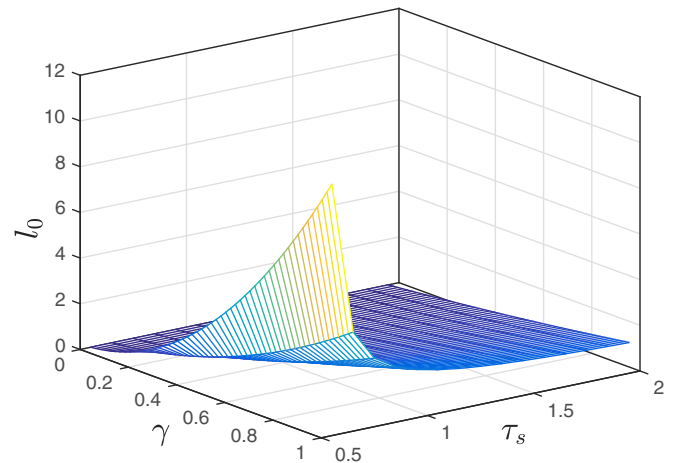

FIG. 6. Dependence of l_0 on γ and τ_s. The variable l_0 is defined as $l_0 = \frac{\gamma^2 + \gamma(2\tau_s - 1)}{2\tau_s - 1}$.
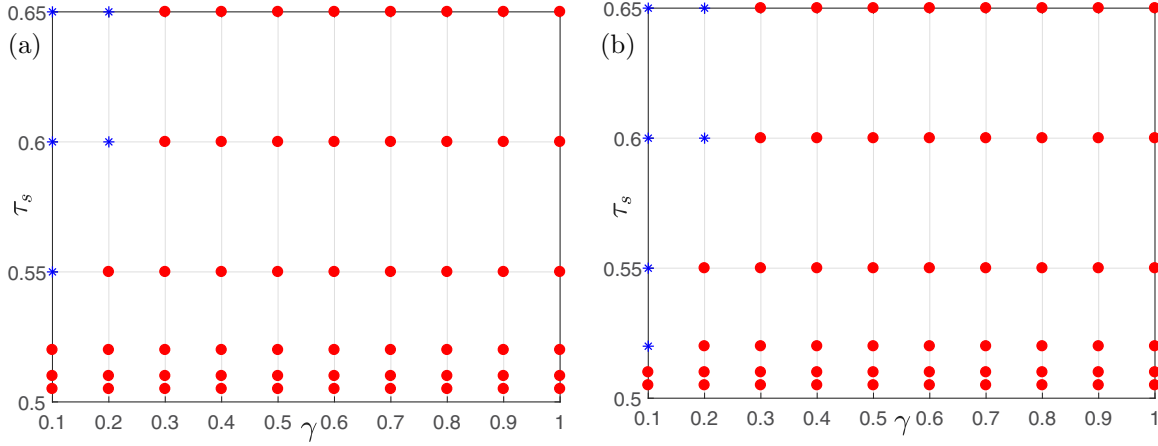
FIG. 7. Work status of code computations against different γ and τ_s at Re = 10 and $M = 20$ for (a) $C = -0.55$ and (b) $C = -0.6$. The filled circles mean that the computations can converge to the steady state, and the asterisks mean that the computations collapse.

the parameter point (γ, τ_s) is marked when the corresponding computation can converge to the steady state or breaks down. As noted above, it can be observed that at a small value of γ, the computations tend to collapse as τ_s increases or C is decreasingly smaller than -0.5. These observations indicate us that to ensure stable code computations, τ_s cannot be far larger than 0.5 and C far smaller than -0.5. During the simulations, we found that the computations will collapse once if $l < -0.4$, and in this case, we hence artificially set $l = 0$ as noted before to balance the simulation accuracy and numerical stability.

2. Inclined channel

In order to test our theoretical analysis for skew boundary geometry, the Poiseuille flow in an inclined channel is further considered. As sketched in Fig. 8, the flat walls are inclined with respect to the underlying grid, and the inclination angle is θ. Here x' and y' are the coordinates, respectively, parallel and perpendicular to the inclined channel wall. Same as the aligned channel, the flow in the inclined channel is periodic from the entrance to the exit. The velocity profiles in the
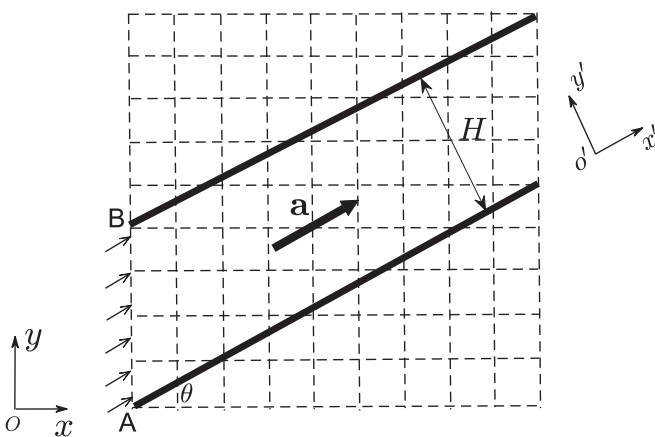

FIG. 8. Schematic illustration of the inclined Poiseuille flow with an inclination angle θ.

inclined channel can be obtained as

$$u = u(y') = 4u_c \frac{y'}{H}\left(1 - \frac{y'}{H}\right), \tag{45}$$

where $y' \in [0, H]$ and $u_c = aH^2/8\nu$.

In the simulations, the computational grid number spanned along the x direction is fixed at $N = 120$. With the lattice size M_{AB} for the segment of AB, the total grid number in the y direction is thus $M = M_{AB} + N\tan\theta$. We performed several simulations with three inclination angles, $\tan\theta = 0.2, 0.5, 1.5$, under different values of M_{AB}. It is stressed that different from the aligned case, the distance ratios γ for boundary nodes herein are not fixed at the same value any longer. For a boundary node with very small γ, if the computed value l by such γ from Eq. (36) is smaller than -0.4, we will, as noted before, set the corresponding parameter l to be zero in the boundary scheme. Figure 9 delineates the velocity profiles of the flow in the inclined channel at Re = 20. As clearly seen from these figures, the numerical predictions from the boundary scheme (15) with Eqs. (36) and (37), and even with the artificial setting for the value of l at very small γ, are all in excellent agreement with the analytical solution. The results obtained by the HBB scheme with Eq. (40) are also presented for comparison. Grid-dependent deviations from the analytical solution are clearly observed. This indicates that even if Eq. (40) is satisfied to yield uniform τ_q, the discrete effects on the HBB scheme, as noted in Sec. III, cannot be eliminated. The intrinsic reason for this is that Eq. (40) adhered to the HBB scheme is derived based on the half-way bounce assumption ($\gamma = 1/2$), which is valid for aligned channel flows but fails for inclined cases. In contrast, by employing Eqs. (36) and (37) for the boundary scheme (15), the discrete effect can be significantly removed with a uniform relaxation time τ_q even at a coarse gird resolution.

In theory, the adjustability of l in the scheme (15) can yield infinite boundary schemes. However, as revealed in Eq. (33), the discrete effects of these boundary schemes will be affected by the values of l. To examine the effect of l on the slip velocity, we take four choices of l ($l = \gamma, 2\gamma, \gamma^2$, and $\gamma^2 + \gamma$) as well as the value of l obeying our derivation (36). Simulations under these cases of l are conducted on
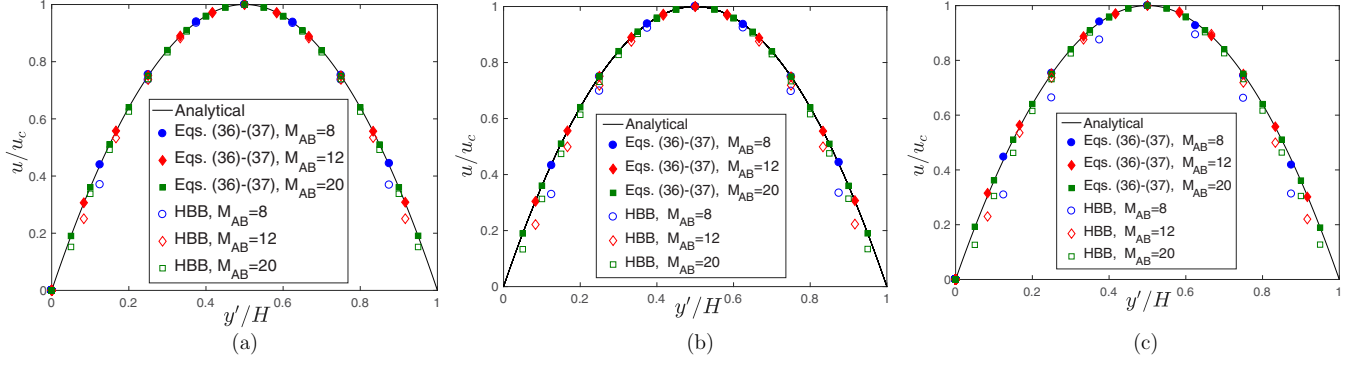
FIG. 9. Velocity profiles of the inclined channel flow under different lattice sizes at Re = 20. Filled shapes denote the results predicted by the boundary scheme (15) with Eqs. (36) and (37). Empty shapes denote the results predicted by the HBB scheme with Eq. (40). (a) $\tan\theta = 0.2$, (b) $\tan\theta = 0.5$, and (c) $\tan\theta = 1.5$.

the same $N_{AB} = 10$ and τ_q determined with Eq. (37) together with $\tau_s = \tau_q$ and $C = -0.55$. As shown in Fig. 10, the flow velocities predicted by the four considered l all depart from the analytical solution, as expected. This is because, based on our theoretical analysis, the four values of l cannot bring uniform relaxation times τ_q to ensure the slip velocity $U_s = 0$. By contrast, the results with the parameter l determined by Eq. (36), and even with several artificial zero values of l for very small γ, show the best robust agreement with the analytical solution. Furthermore, as the inclination angle θ ($\tan\theta$) increases, the deviations from the analytical solution are more pronounced when the parameter l disobeys Eq. (36).

B. Couette flow between two concentric cylinders

To validate the present analysis for more complex geometries, the Couette flow between two rotating concentric cylinders is investigated. This classical flow has been adopted by many researchers as a benchmark problem with curved boundaries [35–39]. The configuration of the flow is shown in Fig. 11, where the inner and outer cylinders have radii R_1 and R_2 and rotate with angular velocities ω_1 and ω_2, respectively. For this problem at steady state, the tangential velocity u_θ

satisfies the following simplified Navier-Stokes equation in cylinder polar coordinates:

$$\frac{d^2 u_\theta}{dr^2} + \frac{d}{dr}\left(\frac{u_\theta}{r}\right) = 0, \tag{46}$$

where (r, θ) is the polar coordinate and r is the radial distance. Under the boundary condition specified above, the analytical solution for this problem can be solved as follows:

$$u_\theta(r) = \frac{\omega_2 - \omega_1 \beta^2}{1 - \beta^2} r + \frac{\omega_1 - \omega_2}{1 - \beta^2} \frac{R_1^2}{r}, \tag{47}$$

where $\beta = R_1/R_2$ and $R_1 \leqslant r \leqslant R_2$.

In our simulations, the two cylinders are placed at the center of a square region resolved by M grid cells. Obviously, the two curved boundary geometries both bring different distance ratios γ at boundary nodes of the inner and outer cylinders. When the very small γ brings $l < -0.4$ from Eq. (36), we will employ the artificial value of $l = 0$ as done in the above problem. As the rotation of the two cylinders is concerned, there are three cases of cylindrical flows for the problem: a stationary outer cylinder and a rotating inner cylinder (case I); second, a stationary inner cylinder and a rotating outer
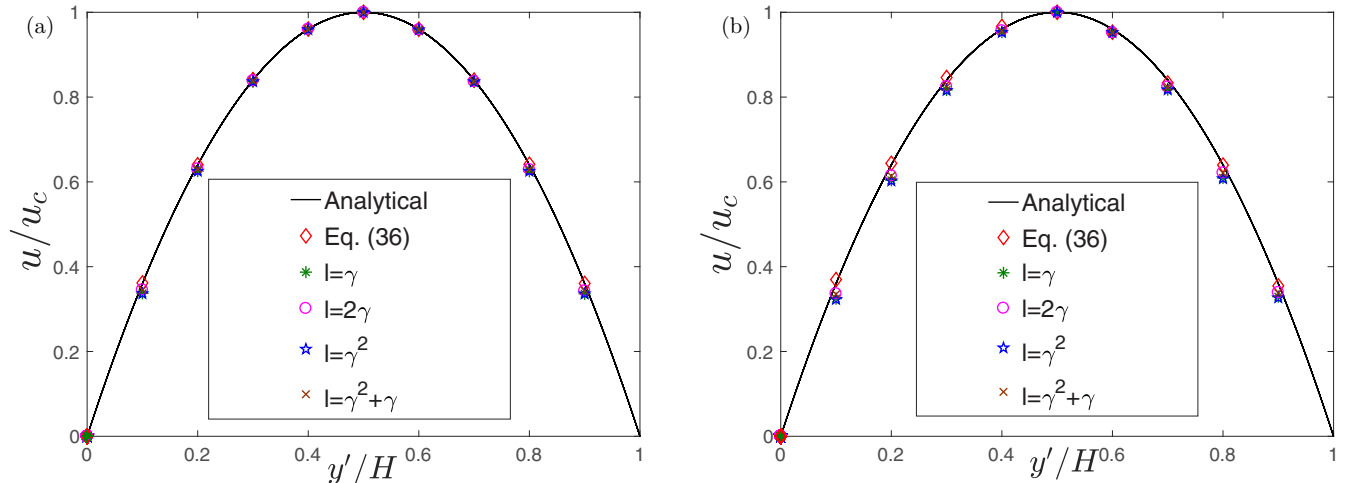

FIG. 10. Velocity profiles of the inclined channel flow predicted under different cases of l at $M_{AB} = 10$ and Re = 20. (a) $\tan\theta = 0.5$ and (b) $\tan\theta = 1.5$.
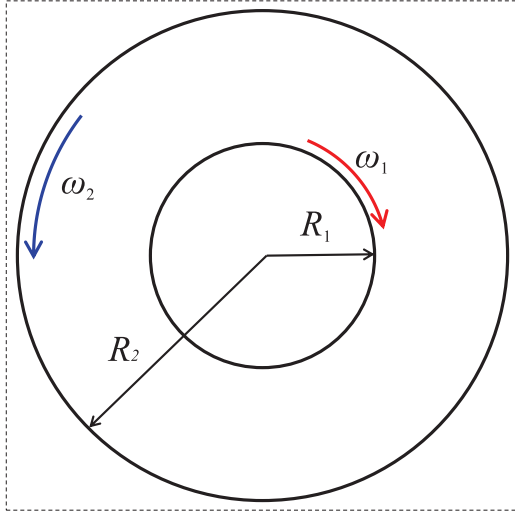
FIG. 11. Schematic illustration of the circular Couette flow.

cylinder (case II); and, third, rotating inner and outer cylinders (case III). A number of simulations for the three cases are conducted to predict the velocity profiles with different values of M and β. The kinematic viscosity ν and the corresponding relaxation time τ_s are fixed at $\nu = 0.01$, $\tau_s = 0.65$. Different values of β are obtained by changing R_1 under a fixed $R_2 = 1.0$. In Fig. 12 the numerical results obtained by the scheme (15) with Eqs. (36) and (37) are shown together with those from the HBB scheme with Eq. (40) for comparison. For the three cases with different lattice sizes, one can see that the HBB scheme with Eq. (40) yields apparent grid-dependent discrepancies from the analytical velocity profiles. In contrast, good agreements with the analytical solutions are found for the simulation results by the scheme (15) with Eqs. (36) and (37). This again strengthens and demonstrates our theoretical analysis to eliminate the discrete effects of curved boundary conditions.

The parameter l are also investigated on the discrete effects from curved boundary conditions. As done before, four choices of l besides Eq. (37), i.e., $l = \gamma$, 2γ, γ^2, and $\gamma^2 + \gamma$, are examined, and τ_q is equally given by Eq. (37) with $C = -0.6$. As has been studied by Schlichting [40], the ratio β has

a strong influence on the variation of the velocity profile for case I, while for case II, its effect is negligible for the velocity profile. Thus, we simulated the cylindrical flows of case I where $\omega_1 = 0.02$, $\omega_2 = 0$. Figure 13 compares the simulated velocities corresponding to the above values of l at $M = 18$. In contrast with the good and robust predictions achieved for the case that l is determined by Eq. (36), it is seen again as in Fig. 10 that the numerical predictions with other choices of l display obvious deviations from the analytical solution. The reason for this is due to the fact that the velocity slip U_s cannot be removed for these cases of l.

V. CONCLUSIONS

In this work, the discrete effects on boundary conditions for curved no-slip walls have been analyzed in the framework of the MRT model for fluid flows. Different from previous curved boundary schemes only containing the distance ratio γ, a single-node boundary scheme which incorporates an additional free parameter l besides γ is adopted in the theoretical analysis. The results clearly show that unlike previous theoretical derivations, the slip velocity is affected by the free parameter l combined with the distance ratio γ and the relaxation times (τ_s and τ_q). With the aid of l, we further theoretically provide a strategy to obtain the uniform relaxation time τ_q while the numerical slip can be eliminated successfully. It is also indicated that without the free parameter l besides γ, the discrete effects cannot be removed with a uniform relaxation time τ_q for previous curved boundary conditions and the HBB boundary condition.

Several benchmark problems, including the aligned and inclined channel flows and the cylindrical Couette flow, are simulated to examine the theoretical analysis in this work. In view of the numerical stability at very small γ, the artificial zero value is assigned for l at some boundary nodes. Consistent with the theoretical analysis, the numerical results predicted by our derivation show the best and robust agreement with the analytical solution even with a coarse grid resolution. In contrast, for the HBB scheme and previous curved boundary schemes which contain only γ, grid-dependent deviations from the analytical solution are clearly observed for fluid flows with curved boundaries.
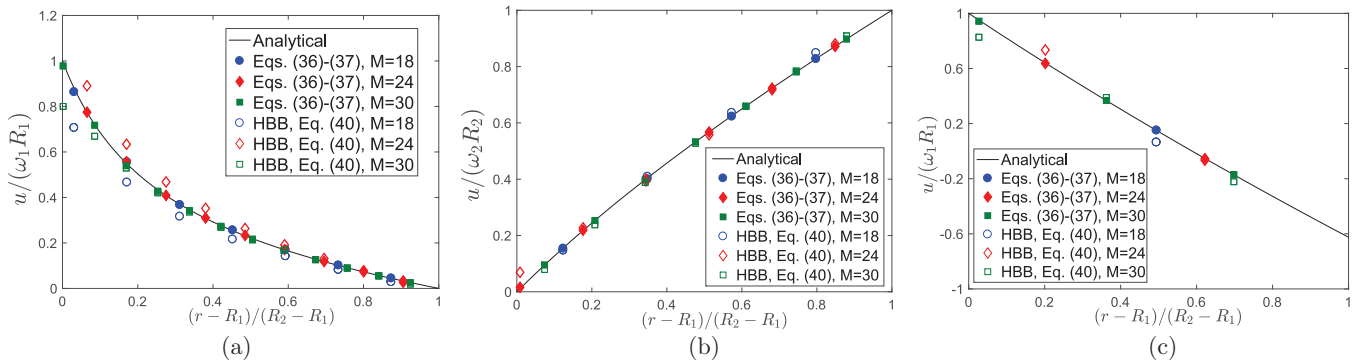

FIG. 12. Velocity profiles of the cylindrical Couette flow for three cases: (a) $\beta = 0.2$, $\omega_1 = 0.02$, $\omega_2 = 0$; (b) $\beta = 0.5$, $\omega_1 = 0$, $\omega_2 = 0.02$; and (c) $\beta = 0.8$, $\omega_1 = 0.02$, $\omega_2 = -0.01$. Filled shapes denote the results from the scheme (15) with Eqs. (36) and (37) ($C = -0.6$). Empty shapes denote the results predicted by the HBB scheme with Eq. (40).
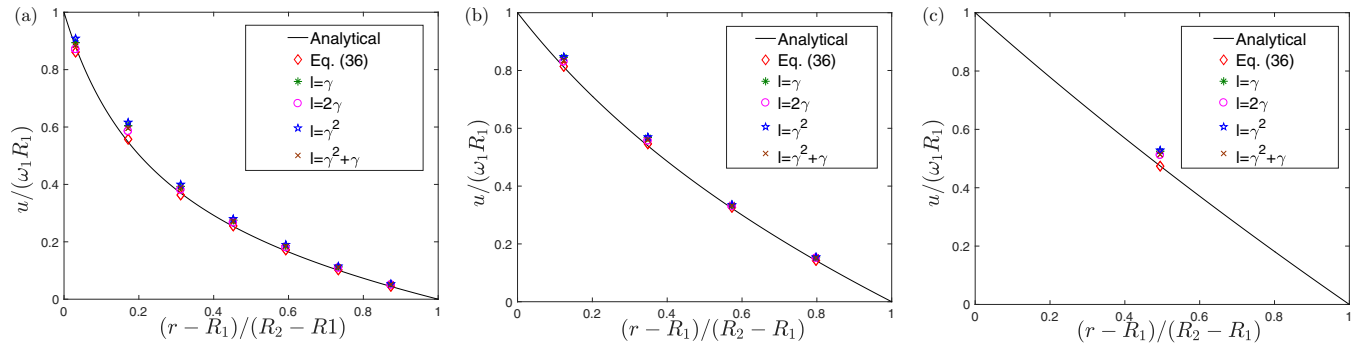
FIG. 13. Velocity profiles of the cylindrical Couette flow under (a) $\beta = 0.2$, (b) $\beta = 0.5$, and (c) $\beta = 0.8$ at $M = 18$.

The present study also demonstrates that when eliminating the numerical slip on curved no-slip walls, adding free parameters to the boundary condition is an effective strategy to ensure the uniform relaxation times. Actually, in addition to the present work, we have conducted a similar theoretical analysis on curved boundary conditions within the MRT model based on the lattice kinetic scheme [17,20]. It is again found that although more relaxation parameters are included in the slip velocity derived from a curved boundary condition containing only γ, the relaxation time τ_q still changes locally with γ to eliminate the slip velocity.

The theoretical derivations in this work show that the slip velocity of curved boundary conditions can be successfully eliminated by the proposed treatment with uniform relaxation parameters. For practical problem simulations, we would note

that the numerical stability should be considered for the free parameter l at small values of γ. Finally, the present analysis is limited to two-dimensional flow problems, while its extension to the three-dimensional case would not be so difficult. Such work will be addressed in the future.

[1] S. Y. Chen and G. D. Doolen, Annu. Rev. Fluid Mech. **30**, 329 (1998).
[2] C. K. Aidun and J. R. Clausen, Annu. Rev. Fluid Mech. **42**, 439 (2010).
[3] Q. Li, K. H. Luo, Q. J. Kang, Y. L. He, Q. Chen, and Q. Liu, Prog. Energy Combust. **52**, 62 (2016).
[4] M. Maxey, Annu. Rev. Fluid Mech. **49**, 171 (2017).
[5] J. Zhang, Microfliud. Nanofluid. **10**, 1 (2011).
[6] H. Liang, Y. Li, J. Chen, and J. Xu, Int. J. Heat Mass Transf. **130**, 1189 (2019).
[7] S. Succi, *The Lattice Boltzmann Equation for Fluid Dynamics and Beyond* (Oxford University Press, Oxford, 2001).
[8] Z. L. Guo and C. Shu, *Lattice Boltzmann Method and Its Applications in Engineering* (World Scientific, Singapore, 2013).
[9] T. Kruger, H. Kusumaatmaja, A. Kuzmin, O. Shardt, G. Silva, and E. M. Viggen, *The Lattice Boltzmann Method*, Graduate Texts in Physics (Springer, Cham, 2017), pp. 297–329.
[10] I. Ginzburg and P. M. Adler, J. Phys. II (France) **4**, 191 (1994).
[11] X. He, Q. Zou, L.-S. Luo, and M. Dembo, J. Stat. Phys. **87**, 115 (1997).
[12] N. I. Prasianakis, T. Rosen, J. Kang, J. Eller, J. Mantzaras, and F. N. Buchi, Commun. Comput. Phys. **13**, 851 (2013).
[13] J. P. Meng, X.-J. Gu, and D. R. Emerson, J. Comput. Sci. **28**, 476 (2018).
[14] F. Dubois, ESAIM **18**, 181 (2007).

[15] F. Dubois, Comput. Math. Appl. **55**, 1141 (2008).
[16] F. Dubois, P. Lallemand, and M. M. Tekitek, Comput. Math. Appl. **59**, 2141 (2010).
[17] T. Inamuro, Philos. Trans. R. Soc. London A **360**, 477 (2002).
[18] X. G. Yang, B. C. Shi, and Z. H. Chai, Phys. Rev. E **90**, 013309 (2014).
[19] L. Wang, W. F. Zhao, and X. D. Wang, Phys. Rev. E **98**, 033308 (2018).
[20] X. H. Meng and Z. L. Guo, Phys. Rev. E **92**, 043305 (2015).
[21] S. K. P. Sanjeevi, A. Zarghami, and J. T. Padding, Phys. Rev. E **97**, 043305 (2018).
[22] J. Bao, Y. Peng, and L. Schaefer, J. Comput. Phys. **227**, 8472 (2008).
[23] O. Oulaid and J. F. Zhang, Eur. J. Mech. B **53**, 11 (2015).
[24] M. Rohde, D. Kandhai, J. J. Derksen, and H. E. A. Van den Akker, Phys. Rev. E **67**, 066703 (2003).
[25] O. Filippova and D. Hanel, J. Comput. Phys. **147**, 219 (1998).
[26] R. Mei, L. Luo, and W. Shyy, J. Comput. Phys. **155**, 307 (1999).
[27] I. Ginzburg and D. d'Humieres, Phys. Rev. E **68**, 066614 (2003).
[28] A. J. C. Ladd, J. Fluid Mech. **271**, 311 (1994).
[29] A. J. C. Ladd and R. Verberg, J. Stat. Phys. **104**, 1191 (2001).
[30] D. Kandhai, A. Koponen, A. Hoekstra, M. Kataja, J. Timonen, and P. M. A. Sloot, J. Comput. Phys. **150**, 482 (1999).

[31] W. F. Zhao, J. T. Huang, and W.-A. Yong, Multiscale. Model. Simul. **17**, 854 (2019).

[32] C. Pan, L.-S. Luo, and C. T. Miller, Comput. Fluids **35**, 898 (2006).

[33] P. Lallemand and L. S. Luo, Phys. Rev. E **61**, 6546 (2000).

[34] L. Wang, Z. L. Guo, B. C. Shi, and C. G. Zheng, Commun. Comput. Phys. **13**, 1151 (2013).

[35] W. F. Zhao and W.-A. Yong, J. Comput. Phys. **329**, 1 (2017).

[36] Z. L. Guo, C. G. Zheng, and B. C. Shi, Phys. Fluids **14**, 2007 (2002).

[37] O. R. Mohammadipour, S. Succi, and H. Niazmand, Phys. Rev. E **98**, 023304 (2018).

[38] Y. T. Chew, C. Shu, and Y. Peng, J. Stat. Phys. **107**, 539 (2002).

[39] S. B. Di and W. Ge, Particuology **18**, 22 (2015).

[40] H. Schlichting, *Boundary-Layer Theory* (McGraw-Hill, New York, 1979).